Porous Si/Cu6Sn5/C composite containing native oxides as anode material for lithium-ion batteries

Yawen He, Zhongbin Ye, Mohamad Chamas, Moulay Tahar Sougrati, Pierre-Emmanuel Lippens

To cite this version:

Yawen He, Zhongbin Ye, Mohamad Chamas, Moulay Tahar Sougrati, Pierre-Emmanuel Lippens. Porous Si/Cu6Sn5/C composite containing native oxides as anode material for lithium-ion batteries. Journal of Materials Science: Materials in Electronics, 2022, 33, pp.235-243. ⟨10.1007/s10854-021-07288-1⟩. ⟨hal-03415279⟩

HAL Id: hal-03415279
https://hal.science/hal-03415279v1

Submitted on 4 Nov 2021

Porous Si/Cu_6Sn_5/C composite containing native oxides as anode material for lithium-ion batteries

Yawen He[a,b,*], Ye Zhongbin[a], Mohamad Chamas[a], Moulay Tahar Sougrati[b], Pierre-Emmanuel Lippens[b]

[a] School of Chemistry and Chemical Engineering, Southwest Petroleum University,

Chengdu 610500, China

[b] Institut Charles Gerhardt, UMR 5253 CNRS, Université de Montpellier,

Place Eugène Bataillon, 34095 Montpellier cedex 5, France

*Corresponding author：*yawenhe0622@gmail.com*

Abstract

Porous Si/Cu_6Sn_5/C composite containing native oxides was prepared via solid state mechanical milling and wet chemical etching. This composite was used as anode material for Li-ion batteries. X-ray diffraction, electron microscopy, ^{119}Sn Mössbauer spectroscopy and X-ray photoelectron spectroscopy show that the composite has a pitaya-like morphology based on porous Si and embedded Cu_6Sn_5 non-porous microparticles with surface native oxides. Both Si and Cu_6Sn_5 are electrochemically active and the activation process during the first charge-discharge cycles improves the nanostructuration of the composite that helps to buffer the volume variations of the Li-Si and Li-Sn alloying reactions. The porous composite delivers a reversible and stable capacity of 900 mAh.g^{-1} at a galvanostatic current density of 422 mA.g^{-1} with a retention of 90% for 100 cycles, which is higher than porous Si (53%). The stability during cycling is explained by buffering effects, enhanced electrode conductivity and stable SEI due to the presence of native oxides and the use of FEC-containing electrolyte.

Key words: porous Si composite, anode, passivation

1. Introduction

Silicon is a promising anode material with a high specific capacity (4200 mAh.g^{-1}) for lithium-ion batteries. However, Si suffers from severe problems of volume expansion (~300%) when lithiated. The use of porous or nanosized structures of Si [1] is an efficient way to reduce the effects of volume expansion of electrode materials. Due to the poor intrinsic conductivity of Si [2] and volume expansion during lithiation, carbon coating could enhance the conductivity and buffer Si expansion but the technical process involves wet chemical treatment [3]. To simplify the procedure of synthesis, metals or alloys are preferred to make Si-based composites for lithium-ion battery anodes. Researchers have fabricated different forms of porous Si/Cu [4] composites using Cu as passivation and conductive matrix, leading to good cycling performance. But the synthetic steps are complex. Cu_6Sn_5 shows a theoretical capacity of 600 mAh.g^{-1} and could be an active matrix delivering extra reversible capacity. The lithiation of Cu_6Sn_5 contributes to the extrusion of Cu [5], which increases the matrix conductivity. The idea of this work is to decrease the Si content in the composite by addition of Cu_6Sn_5 and carbon. In that case, the volume expansion of the electrode could be largely decreased. Meanwhile, Cu_6Sn_5 could provide an extra capacity with the formation of Li_xSn.

One usually distinguishes insertion, alloying and conversion reactions as basic lithiation mechanisms of anode materials for Li-ion batteries. The intercalation materials have usually rather low capacity due to the limited number of lithium that can be inserted into the host structure. For example, the commonly used graphite anode material can only intercalate 1 Li for 6 C between the layers, leading to the capacity of 372 $mAh.g^{-1}$. Other insertion materials such as titanates provide enhanced safety and fast charge capabilities but also show rather low capacity [6, 7]. Higher capacities can be obtained with conversion [8, 9] or alloying materials that involve more lithium per electroactive element but with strong structural modifications. For example, the alloying materials Si and Sn can reversibly react with up to 4.4 lithium per element to form $Li_{4.4}Si$ (4200 $mAh.g^{-1}$) and $Li_{4.4}Sn$ (1000 $mAh.g^{-1}$), respectively, but with strong volume changes of several hundred percent [10]. The alloying reaction of Si particles with lithium gives amorphous Li_xSi [11], and then crystalline $Li_{14}Si_5$ [12]. The η-Cu_6Sn_5 crystalline particles first react with lithium with the formation of the Li_2CuSn phase and extrusion of Cu atoms. Then, there is a two-step process involving the progressive lithiation of Li_2CuSn with Cu extrusion followed by the transformation into $Li_{4.4}Sn$ [5,13–15]. The charge is based on the dealloying reaction of $Li_{4.4}Sn$ and back reaction with Cu for form Li_2CuSn, which is then transformed into Cu_6Sn_5 [14,15]. Moreover, the as-synthesized Cu_6Sn_5 was generally reported with oxidized surface in form of SnO_2 [16] that is electrochemically active [17].

In this work, we show that a porous Si/Cu_6Sn_5/C composite can be synthesized by using mechanical milling and wet chemical etching. Chemical etching was used to produce porosity as well as nanostructured Si with embedded Cu_6Sn_5 particles. The composite is described from measurements by X-ray diffraction (XRD), X-ray photoelectron spectroscopy (XPS), electron microscopy and ^{119}Sn Mössbauer spectroscopy. Finally, we show that the composite provides a capacity of 900 $mAh.g^{-1}$ and a better capacity retention during galvanostatic cycling than porous Si.

2. Experimental

Synthesis. Cu_6Sn_5 was prepared via solid state reaction route by using exact stoichiometric ratio of Cu (3 μm, analytical pure 99.99%, Aladdin Co. Ltd) and Sn (5 μm, analytical pure 99.99%, Aldrich) under Ar/H_2 (95/5) flow protection at 350ºC for 5 h. Afterwards, $Al_{80}Si_{20}$ (5μm, Hunan 369 Metallurgical Technology Co., Ltd), synthetized Cu_6Sn_5 and carbon (by mass ratio 5:13:2) were mixed into 100 mL pot under Ar atmosphere for 36 h ball milling (balls/powder mass ratio:1/30). Then, 1.0 g of the $Al_{80}Si_{20}$/ Cu_6Sn_5/ C composite was immersed in to 2.0 M HCl solution with N_2 flow for 4 h. After filtration, the obtained powder was dried in the oven at 80ºC for overnight.

Characterization. The synthesized powder was stored in the Ar-filled glove box. The powder was taken out of the glove-box with the Ar protection setup just before the measurements. X-ray diffraction was carried out by an X-Pert PRO machine (Malvern Panalytical) using under CuK_α radiation λ =0.154056 nm. The morphology of the materials was characterized by field emission scanning electron microscopy (SEM, FEI InspectF50, accelerating voltage 200 V-30 kV) and transmission electron microscopy (TEM, FEI Tecnai G2 F30). The ^{119}Sn Mössbauer spectroscopy was used for the identification of the tin phases within the pristine powder. The measurements were performed at 300 K with an absorber thickness of ~25 $mg.cm^{-2}$. X-ray photoelectron spectroscopy (XPS) was used with Al K_α X-ray source (1486.68 eV) under the voltage of 15 kV and current of 10 mA. The XPS measurements were carried out with a vacuum degree of $5*10^{-10}$ Pa. The binding energy scale was calibrated from the carbon contamination using the C 1s peak at 284.8 eV. N_2-isotherm measurements were performed with 3Flex Micromeritics Instrument Corp. The powder material (~150 mg) was dried at 100ºC and degassed at 200ºC.

Electrochemistry. The composite was mixed with binder carboxy methylcellulose (CMC, Mw=250,000) and carbon by mass ratio of 70/17/13. The mixture was ball milled for 30 min, casted onto Cu foil and dried in oven under vacuum for 4 hours at 120ºC. The loading mass for electrode is approximately 1 $mg.cm^{-2}$. Coin cells (type CR2032) were assembled with lithium foil as counter electrode and microporous Whatman separator (GF/A 1820-047) under argon filled glove box. Electrolyte was 1.0 M $LiPF_6$ in (EC/DEC) + 2 vol% VC + 10 vol% FEC. Galvanostatic electrochemistry cycling tests were performed with voltage cut-off 0.05 - 1.2 V versus Li/Li^+ (Neware BTS4000) at 25°C. Electrochemical impedance spectroscopy (EIS) measurements were carried out with the SP-50 electrochemical station (Biologic Ins.) and a three-electrode Swagelok cell.

3. Results and Discussion

Figure 1a shows the XRD patterns of the as-synthesized composites before etching: $Al_{80}Si_{20}/Cu_6Sn_5/C$, and after etching: $Si/Cu_6Sn_5/C$. The peaks of $Al_{80}Si_{20}$ can be assigned to Al (*Fm*-3*m*) and Si (*Fd*-3*m*) crystalline phases. As removal of Al by HCl, the broad peak at 28.3° can be assigned to Si (*Fd*-3*m*) with crystallite size of 12 nm as evaluated by the Scherrer's equation. The typical peaks of as-synthesized Cu_6Sn_5 belong to monoclinic phase *C2/c*. The additional peaks at 30.7 and 32.2° are assigned to βSn. After etching, Al and Sn were dissolved in HCl solution [18]. In Fig. 1b, the composite shows spherical nanostructured particles. The connection, porosity and contact-embedded structure of Si and Cu_6Sn_5 are proved in Fig.1c, 1d and 1e, respectively.

The N_2 isotherm curves and average pore width distribution of the composite are shown in Fig. 2a, giving a surface area of 30 $m^2.g^{-1}$ and an average pore size of 15 nm. The decrease of the specific surface area compared to $Al_{80}Si_{20}$ is due to non-porous Cu_6Sn_5. Simultaneously, the average particle pore width shows a slight change that reflects the pore size of porous Si, which is also consistent with the SEM image. The ^{119}Sn Mössbauer spectra of the composite before and after etching were successfully fitted to two doublets (Fig. 2.b). In both samples, the unresolved doublet at about 2.2 $mm.s^{-1}$ with a quadrupole splitting of 0.66 $mm.s^{-1}$ can be assigned to Cu_6Sn_5. The other doublet at approximately 0 mm/s with quadrupole splitting of 0.64 $mm.s^{-1}$ is attributed to SnO_2 at the surface of tin based particles [19]. The absorption area ratio of η-Cu_6Sn_5/SnO_2 is = 9 before etching and = 2 after etching, which could be due to the etching process [18]. This is also consistent with the oxidation of Sn in H_2O containing HCl solution. By considering that the Lamb-Mössbauer factor of Cu_6Sn_5 relative to SnO_2 is 0.4 at 300 K [20], the Sn atomic ratio in η-Cu_6Sn_5/SnO_2 is 22 before etching and 5 after etching, which confirms the strong oxidation of the tin phases during etching.

The XPS measurements of as-synthesized Cu_6Sn_5 and $Si/Cu_6Sn_5/C$ composite were performed at the same time in the same chamber (Fig. 3). The Cu 2p and Sn 3d spectra of the as-synthesized Cu_6Sn_5 clearly exhibit two main components due to spin-orbit at binding energies (BE): BE = 932.5 eV / 952.5 eV and 485.1 eV / 493.4 eV corresponding to Cu^0 and Sn^0, respectively (Fig. 3a). The Sn 3d and O 1s XPS components at BE = 487.0 eV / 495.4 eV (Sn^{4+}) and 530.7 eV / 532.3 eV, respectively, reflect surface oxidation due to the exposure of the sample in air. The Cu 2p spectrum of the Si/Cu_6Sn_5/C composite was fitted to a doublet at BE = 934.7 eV / 954.6 eV (Cu^{2+}) corresponding to CuO, as confirmed by the satellite peaks at BE = 943 eV / 963 eV due to the unfilled $3d^9$ state in CuO [21], and to a doublet at BE = 932.5 eV / 952.4 eV (Cu^+) that can be attributed to Cu_2O. The two main peaks of the Sn 3d spectrum at 487.0 eV/ 495.4 eV are due to Sn^{4+} in SnO_2 and the two small peaks at 485.1 eV / 493.4 eV to Sn^0 in Cu_6Sn_5. Thus, both Cu 2p and Sn 3d spectra show the strong oxidation of the surface of the Cu_6Sn_5 particles, in agreement with Mössbauer spectra but not observed by XRD due to the amorphous nature of the oxides. Before etching, the surface oxides or hydroxides were detected because of the absorbed molecules or surface oxidation. After etching, the Sn^0 is not detectable by XPS, because the ball milling process changed the elemental distribution of Si/Cu/Sn elements as suggested by the SEM-EDS images (the pitaya-like structure) and the surface of Cu_6Sn_5 was oxidized during ball milling and etching process. The surface atomic compositions obtained from the XPS survey spectra are given in Table 1. The observed high relative amount oxygen also reveals the surface oxidation of the particles.

In Fig. 4a, the voltage profile of porous Si in Li half-cell shows a decrease from 1.2 to 0.6 V at the beginning of discharge due to the reduction of native oxides and the formation of a solid electrolyte interphase (SEI) resulting from the electrolyte degradation. The slightly sloppy plateau at about 0.2 V-0.05 V corresponds to the lithiation of Si. The 1st discharge shows a specific capacity of 3000 $mAh.g^{-1}$, which corresponds to the composition $Li_{3.1}Si$. This is because the voltage cut-off was fixed at 0.05 V vs. Li/Li^+. In Fig. 4b, the voltage profile of Si/Cu_6Sn_5/C shows the SEI formation and reduction of oxides (CuO, SiO_y, SnO_2) until about 0.5 V, a 1st plateau at about 0.35 V due to the transformation of Cu_6Sn_5 into Li_2CuSn [16,22], and the second plateau at 0.2 V-0.05 V reflecting the continuous lithiation of Li_2CuSn and Si. The CV curve of porous Si shows the typical peaks of the lithiation of Si: 0.01 V and 0.15 V (from the 2nd cycle) and of its delithiation: 0.40 V / 0.53 V (Fig. 4c) [12]. The same peaks are found in the CV curve of Si/Cu_6Sn_5/C while the additional peak at 0.81 V, corresponding to the voltage plateau at the end of charge (Fig. 4b), reflects the delithiation of the Li-Cu-Sn ternary phase (Fig. 4d) [23]. In summary, the electrochemical mechanism for the first discharge of the composite consists of (i) the irreversible reduction of oxides and formation of the SEI leading to a capacity loss of about 300 $mAh.g^{-1}$, (ii) Cu_6Sn_5 transformation into Li_2CuSn and (iii) alloying reactions of Li_xSi and formation of Li_ySn. During the charge, there are dealloying reactions of Li_xSi and Li_ySn with the formation of amorphous-Si and back-reaction of Li-poor Li_ySn with Cu to form Cu_6Sn_5 at the end of charge.

The comparison of the galvanostatic cycling performance for 100 cycles (C/20 for 3 cycles and then C/3) shows unstable variations and low retention (55%) of the capacity for porous Si while the capacity of Si/Cu_6Sn_5/C composite is more stable with a high retention of 90% (Fig. 5a). This strong capacity fade of porous Si (cycle No. 2-60) could be due to the disconnection of the active particles [24]. To confirm the latter assumption, we evaluated the relative irreversible coulombic efficiency at cycle n: $RIC_{DISCONN} = (C_{Cn}-C_{Cn+1})/C_{Cn}$, where C_{Cn} and C_{Cn+1} are the charge capacities of the n^{th} and $(n+1)^{th}$ cycles, respectively [25]. In Fig. 5b, the variations of the cumulated $RIC_{DISCONN}$ as a function of cycle number show a strong increase for porous Si that proves the loss of electrical contacts during electrode cycling as discussed previously [25]. The low values and the slight increase of the cumulated $RIC_{DISCONN}$ for the composite reflect better electrical contacts. This result is in line with the observed stable capacity of the composite, which can be explained by the stability of the electrode film due to the buffering effect and enhanced electronic conductivity of Cu_6Sn_5, Cu and C particles, and to the SEI stabilization owing to the additives (VC, FEC) of the electrolyte [26,27] and active Si [24].

As shown in Fig. 5a, the coulombic efficiency of porous Si increases from 77 to 98 % for the two first cycles and then shows some small variations, in line with capacity fading due to the loss of electrical contacts, as discussed above, or the aggregation of particles during cycling [24]. For the $Si/Cu_6Sn_5/C$ composite, the first discharge consists of the irreversible reduction of native oxides and SEI formation, followed by reversible formation of Li_xSi and Li_ySn active nanoparticles. Such mechanism requires an activation process, of 3 cycles here, for the gradual nanostructuration of the composite as observed previously for other Si-based composites [28]. As a result, there is a strong increase of the coulombic efficiency from 50% to 92% for the two first cycles, then a gradual increase up to 99% for the following 3 cycles and a stabilization at this value until the end of cycling. The Li consumption due to the activation process could be supported by the pre-lithiation techniques for applications in full-cells [29,30]. Compared to other Si-based electrode materials, the present Si composite has a lower but more stable capacity as reflected by the significantly higher capacity retention (Table 2). Finally, the $Si/Cu_6Sn_5/C$ composite shows a stable rate capability (Fig. 5c).

Additional information that explains the performance of the composite was obtained by XRD and electrochemical impedance spectroscopy (EIS). The cycled electrodes at the voltages of 0.2 V and 0.05 V were characterized by XRD. The pattern obtained at 0.2 V exhibits weak peaks at 28.3° due to Si and at 30.5° / 42.9° that can be assigned to Cu_6Sn_5 (Fig. 6a). The strong decrease of the peak intensity, compared to the pristine material, confirms the lithiation of these two phases. There is another peak located at 43.3° that could be assigned to Cu nanoparticles. Note that changes in the background intensity below 30° are due Kapton used to maintain the powdered sample during XRD measurements. At the voltage of 0.05 V, no peaks of Si or Cu_6Sn_5 are detected, suggesting the almost full lithiation of all the crystalline phases. The only visible but slight peak at 43.3° reflects the existence of Cu nanoparticles that can improve the electronic properties of the composite. The Nyquist plots of the EIS spectra at the end of the 1st and 25th discharges are shown in Fig. 6b. The spectra were fitted with an equivalent circuit that takes into account the resistances of electrolyte (R_1), SEI (R_2) and charge transfer (R_3) (Fig. 6b). From the 1st to the 25th cycle, the electrolyte resistance is constant $R_1 \approx 4\ \Omega$, the SEI resistance decreases from $R_2 = 37$ to $25\ \Omega$ and the charge transfer resistance increases from $R_3 = 7$ to $22\ \Omega$. The values of R_2 and R_3 are smaller than reported values in porous Si/Cu based electrodes [35], which confirms the enhanced electronic percolation within the electrode and the improved Li^+ transportation through the interfaces between the active particles and the electrolyte. This also explains the observed good rate capability of the composite.

4. Conclusion

The porous $Si/Cu_6Sn_5/C$ composite was obtained from $Al_{80}Si_{20}$, Cu_6Sn_5 and C powders by mechanical milling method and wet chemical etching steps for removing Al. This composite shows a porous structure of Si with embedded Cu_6Sn_5 particles. Owing to the porosity and passivation resulting from the etching process, the composite anode shows a reversible capacity of 900 $mAh.g^{-1}$ for a current of 420 $mA.g^{-1}$ with a capacity retention of 90% at the 100th cycle, compared with only 53% for porous Si. The better stability is ascribed to Cu, C and Cu_6Sn_5 particles that help to buffer the volume variations of the Li-Si alloying reactions and enhance the electronic conduction. The passivation from the native oxides and the FEC-containing electrolyte stabilize the SEI and also contribute to the performance of the composite.

Acknowledgements

This work was financially supported by Project of National Natural Science Foundation (NSFC 21650110463), the Southwest Petroleum University key project (KSZ16083) and China scholarship council (CSC) program.

References

1. W. Cao, K. Han, M. Chen, H. Ye, and S. Sang, Electrochim. Acta **320**, 134613 (2019).

2. Z. Yi, N. Lin, Y. Zhao, W. Wang, Y. Qian, Y. Zhu, and Y. Qian, Energy Storage Mater. **17**, 93 (2019).

3. X. T. Cheng Li, Xitao Li, Yan-Zhen Zheng, Jiaojiao Wu, Haiyang Ding, ChemElectroChem **6**, 2517 (2019).

4. L. Cao, T. Huang, Q. Zhang, M. Cui, J. Xu, and R. Xiao, ACS Appl. Mater. Interfaces **12**, 57071 (2020).

5. X. F. Tan, W. Yang, K. Aso, S. Matsumura, S. D. McDonald, and K. Nogita, ACS Appl. Energy Mater. **3**, 141 (2020).

6. T.F. Yi, Y. Xie, Y.R. Zhu, R.S. Zhu, H. Shen, J. Power Sources **222**, 448 (2013).

7. T.F. Yi, J. Mei, P.P. Peng, S. Luo, Compos. B: Eng. **167**, 566 (2019).

8. P. Poizot, S. Laruelle, S. Grugeon, L. Dupont, J.M. Tarascon, Nature **407**, 496 (2000).

9. T.F. Yi, J.P. Qu, X. Lai, X. Han, H. Chang, Y.R. Zhu, Mater. Today Chem. **19**, 100407 (2021).

10. Y. Jin, B. Zhu, Z. Lu, N. Liu, and J. Zhu, Adv. Energy Mater. **7**, 1700715 (2017).

11. M. N. Obrovac and L. J. Krause, J. Electrochem. Soc. **154**, A103 (2007).

12. J. Li and J. R. Dahn, J. Electrochem. Soc. **154**, 156 (2007).

13. X. L. Wang, W. Q. Han, J. Chen, and J. Graetz, ACS Appl. Mater. Interfaces **2**, 1548 (2010).

14. D. Larcher, L. Y. Beaulieu, D. D. MacNeil, and J. R. Dahn, J. Electrochem. Soc. **147**, 1658 (2000).

15. L. Fransson, E. Nordström, K. Edström, L. Häggström, J. T. Vaughey, and M. M. Thackeray, J.

Electrochem. Soc. **149**, 736 (2002).

16. S. Naille, R. Dedryvère, H. Martinez, S. Leroy, P. E. Lippens, J. C. Jumas, and D. Gonbeau, J. Power Sources **174**, 1086 (2007).

17. A. Y. Kim, J. S. Kim, C. Hudaya, D. Xiao, D. Byun, L. Gu, X. Wei, Y. Yao, R. Yu, and J. K. Lee, Carbon N. Y. **94**, 539 (2015).

18. Z. Wang, K. Dong, D. Wang, S. Luo, Y. Liu, Q. Wang, Y. Zhang, A. Hao, C. Shi, and N. Zhao, J. Power Sources **441**, 227191 (2019).

19. B. Gangaja, S. Chandrasekharan, S. Vadukumpully, S. V. Nair, and D. Santhanagopalan, J. Power Sources **340**, 356 (2017).

20. R.C. Reno, M.J. Panunto, J. Electron. Mater. **26**, 11 (1997).

21. K. Cao, H. Liu, W. Li, Q. Han, Z. Zhang, and K. Huang, Small **1901775**, 1 (2019).

22. X. F. Tan, S. D. McDonald, Q. Gu, Y. Hu, L. Wang, S. Matsumura, T. Nishimura, and K. Nogita, J. Power Sources **415**, 50 (2019).

23. Q. G. Han, Z. Yi, Y. Cheng, Y. Wu, and L. M. Wang, RSC Adv. **6**, 15279 (2016).

24. E. Radvanyi, W. Porcher, E. De Vito, A. Montani, S. Franger, and S. Jouanneau Si Larbi, Phys. Chem. Chem. Phys. **16**, 17142 (2014).

25. M. Gauthier, D. Mazouzi, D. Reyter, B. Lestriez, P. Moreau, D. Guyomard, and L. Roué, Energy Environ. Sci. **6**, 2145 (2013).

26. T. Jaumann, J. Balach, U. Langklotz, V. Sauchuk, M. Fritsch, A. Michaelis, V. Teltevskij, D. Mikhailova, S. Oswald, M. Klose, G. Stephani, R. Hauser, J. Eckert, and L. Giebeler, Energy Storage Mater. **6**, 26 (2017).

27. V. Etacheri, O. Haik, Y. Goffer, G. A. Roberts, I. C. Stefan, R. Fasching, and D. Aurbach, Langmuir **28**, 965 (2012).

28. L. Chen, X. Xie, B. Wang, K. Wang, J. Xie, Mater. Sci. Eng. B **131**, 186 (2006).

29. Q. Li, X. Liu, X. Han, Y. Xiang, G. Zhong, J. Wang, B. Zheng, J. Zhou, and Y. Yang, ACS Appl. Mater. Interfaces **11**, 14066 (2019).

30. F. Holtstiege, P. Bärmann, R. Nölle, M. Winter, and T. Placke, Batteries **4**, 1 (2018).

31. Z. Yi, N. Lin, Y. Zhao, W. Wang, Y. Qian, Y. Zhu, and Y. Qian, Energy Storage Mater. (2018).

32. Y. Yang, X. Qu, L. Zhang, M. Gao, Y. Liu, and H. Pan, ACS Appl. Mater. Interfaces **10**, 20591 (2018).

33. B. Rangasamy, J. Y. Hwang, and W. Choi, Carbon N. Y. **77**, 1065 (2014).

34. W. An, B. Gao, S. Mei, B. Xiang, J. Fu, L. Wang, Q. Zhang, P. K. Chu, and K. Huo, Nat. Commun. **10**, 1 (2019).

35. L. Lin, Y. Ma, Q. Xie, L. Wang, Q. Zhang, and D. L. Peng, ACS Nano **11**, 6893 (2017).

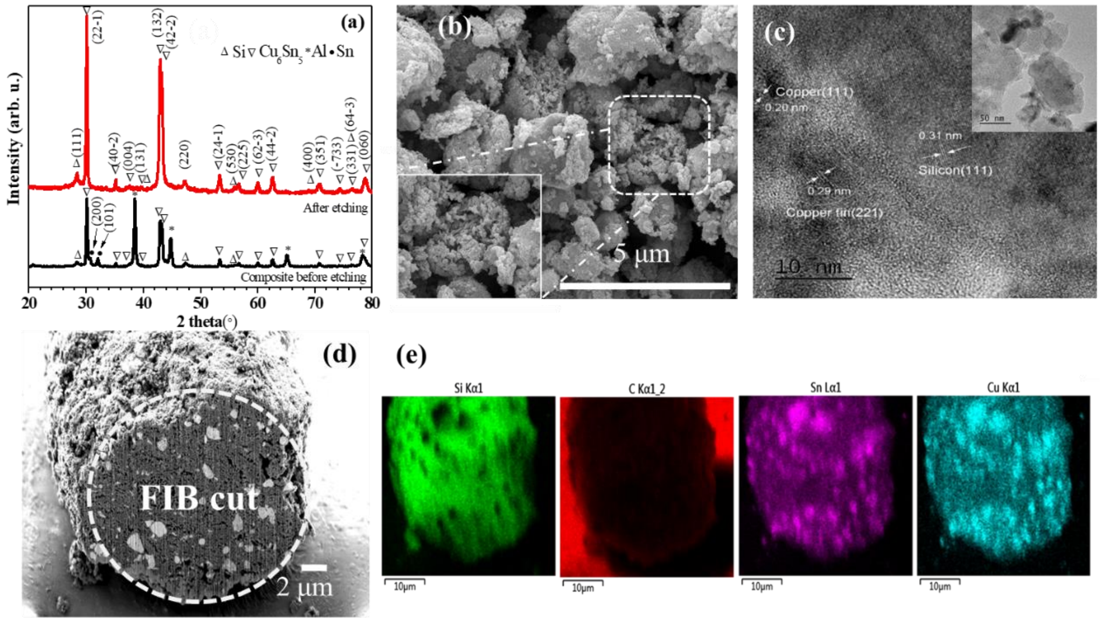

Fig. 1. (a) XRD patterns of $Si/Cu_6Sn_5/C$ composite before and after (porous composite) etching, (b) SEM images of porous $Si/Cu_6Sn_5/C$ composite, (c) TEM image of porous $Si/Cu_6Sn_5/C$ composite (d) FIB image and (e) corresponding EDS images of porous $Si/Cu_6Sn_5/C$ composite.

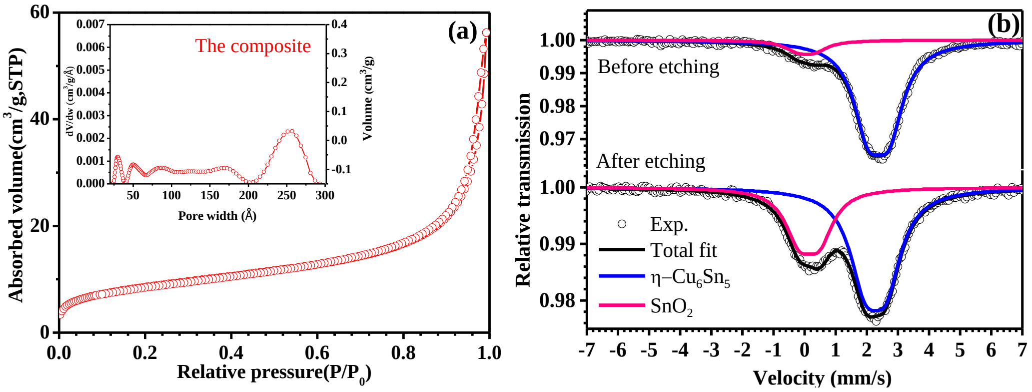

Fig. 2. (a) N_2-isotherm curves (inset: pore width distribution) of porous Si/ Cu_6Sn_5/C composite, (b) ^{119}Sn Mössbauer spectra (300K) of Si/ Cu_6Sn_5/C composite before and after etching

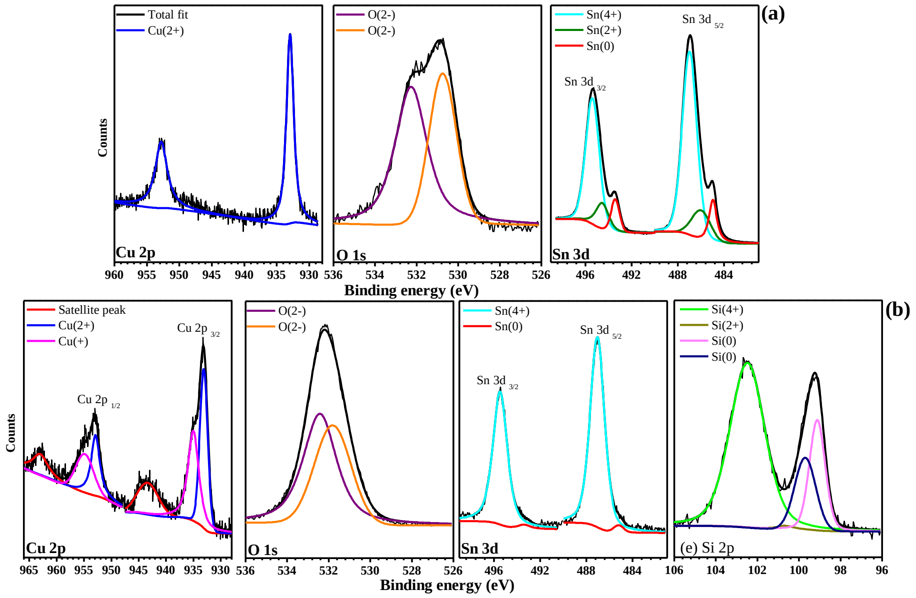

Fig. 3. XPS core-level spectra and fitting curves of (a) as-synthesized Cu_6Sn_5 and (b) porous Si/Cu_6Sn_5/C composite

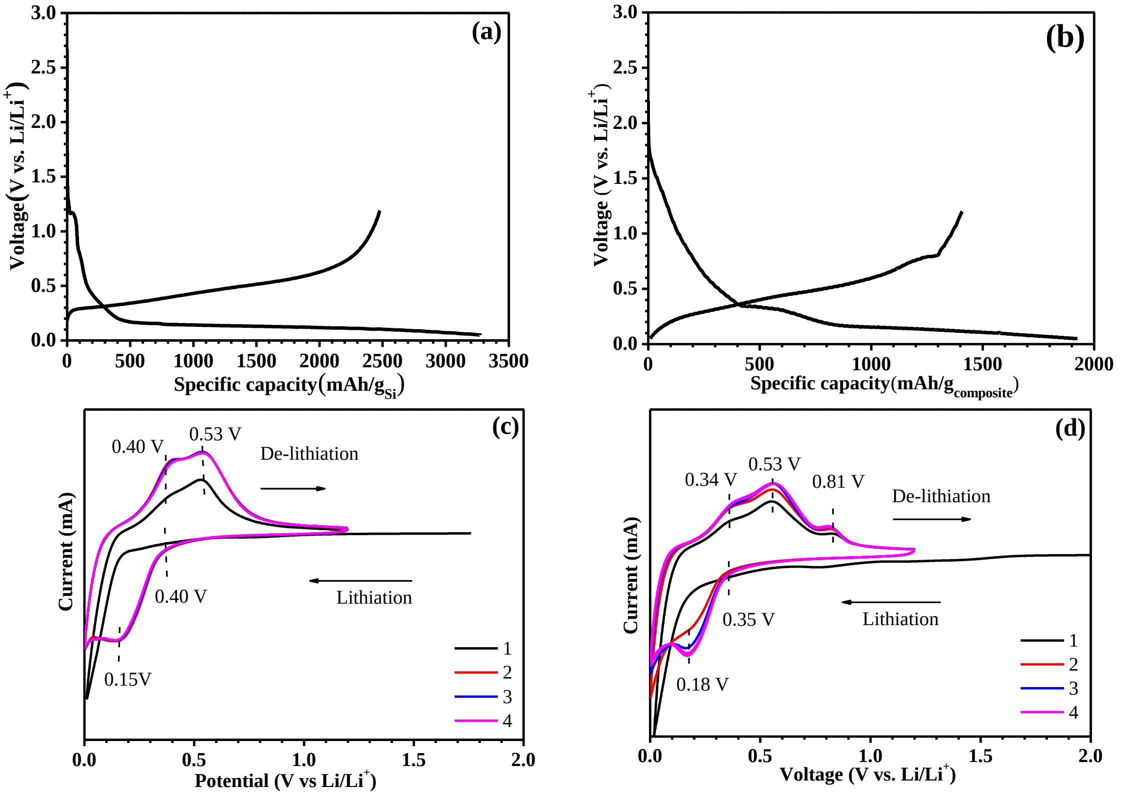

Fig. 4. Voltage curves *vs.* specific capacity of (a) porous Si and (b) porous Si/ Cu_6Sn_5/C composite at C/100. Cyclic voltammetry curves of (c) porous Si and (d) porous Si/ Cu_6Sn_5/C composite at the scan speed of 0.3 mV.s^{-1}.

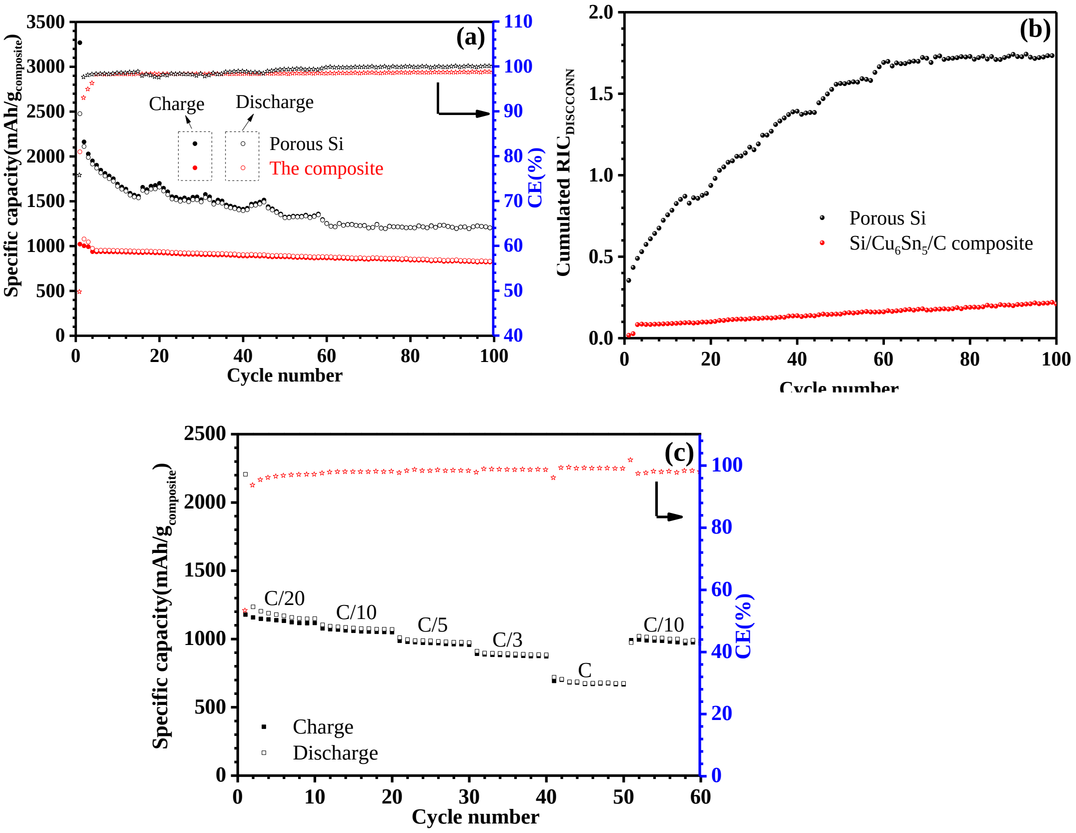

Fig. 5. Electrochemical performance of porous Si and $Si/Cu_6Sn_5/C$ composite: (a) specific capacity and coulombic efficiency vs.cycle number in galvanostatic regime (C/20 for 3 cycles and cycling at C/3), (b) cumulated $RIC_{DISCONN}$ vs. cycle number, and (c) C-rate capability.

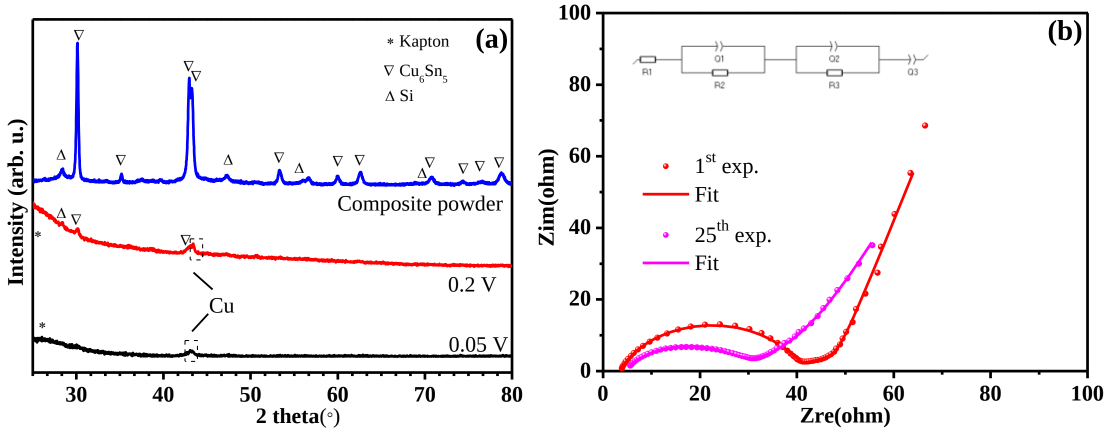

Fig. 6. (a) *Ex-situ* XRD patterns of pristine Si/Cu$_6$Sn$_5$/C composite at different voltages during discharge. (b) Electrochemical impedance spectra of the Si/Cu$_6$Sn$_5$/C composite at the end of the 1st and 25th discharge (inset: equivalent circuit with R1: electrolyte resistance; R2: resistance of SEI; R3: resistance of charge transfer).

Table 1. Atomic composition from XPS survey

Atomic (%)	C 1s	Si 2p	Sn 3d	O 1s	Cu 2p
Cu_6Sn_5	61	-	9	26	4
$Si/Cu_6Sn_5/C$ (after etching)	68	10	1	20	2

Table 2 Comparison between previously published works on Si-based anode materials for Li-ion batteries and the present results.

Composition	Si precursor and synthetic method	Capacity retention (%)	Formulation (Active material: binder: conductive)	Cycling performance
Ball-milled Si [25]	Si, 1-5 µm powder, high-energy ball milling	60	80:12:8	1500 mAhg^{-1} at 50th cycle, 480 mA g^{-1}
Si/CNT composite [31]	Al-Si microsphere, wet chemical method and heat	80	70:15:15	1275 mAh g^{-1} at 100th cycle, 200 mA g^{-1}
Coated Si [32]	Si 2.5 µm powder, pressed ball milling	72	70:20:10	1439 mAh g^{-1} at 100th cycle, 100 mA g^{-1}
Si/CuO/graphene [33]	Si nano powder, wet chemical method and annealing	~71	Not mention	~1100 mAh g^{-1} at 100th cycle, C/2
Bulk porous Si [34]	metallurgical Si 1-3 µm, 3 steps of heat and wet chemical method	~70	80:10:10	~1250 mAh g^{-1} at 100th cycle, C/2
This work	Al-Si 5 µm powder, 2 steps: low speed ball milling and chemical etching	90	70:17:13	830 mAh g^{-1} at 100th cycle, 420 mA g^{-1}